FULL PAPER

Interfacial Sliding and Buckling of Monolayer Graphene on a Stretchable Substrate

Tao Jiang, Rui Huang,* and Yong Zhu*

The nonlinear mechanical response of monolayer graphene on polyethylene terephthalate (PET) is characterised using in-situ Raman spectroscopy and atomic force microscopy. While interfacial stress transfer leads to tension in graphene as the PET substrate is stretched, retraction of the substrate during unloading imposes compression in the graphene. Two interfacial failure mechanisms, shear sliding under tension and buckling under compression, are identified. Using a nonlinear shear-lag model, the interfacial shear strength is found to range between 0.46 and 0.69 MPa. The critical strain for onset of interfacial sliding is ~0.3%, while the maximum strain that can be transferred to graphene ranges from 1.2% to 1.6% depending on the interfacial shear strength and graphene size. Beyond a critical compressive strain of around −0.7%, buckling ridges are observed after unloading. The results from this work provide valuable insight and design guidelines for a broad spectrum of applications of graphene and other 2D nanomaterials, such as flexible and stretchable electronics, strain sensing, and nanocomposites.

1. Introduction

Graphene, the two-dimensional carbon material, has unique electronic, thermal and mechanical properties and holds great promise for a wide range of applications such as nano-electro-mechanical systems,[1–3] flexible/stretchable electronics[4,5] and nanocomposites.[6–8] In particular, with its superior electronic transport properties and high flexibility, graphene is considered one of the emerging materials for next-generation flexible electronics; a variety of graphene-based flexible devices have been demonstrated recently.[9–11] The performance and reliability of these devices are often limited by the interfacial properties between graphene and substrate materials. In this study, we have measured the nonlinear mechanical response of monolayer graphene on top of a commonly used plastic substrate,
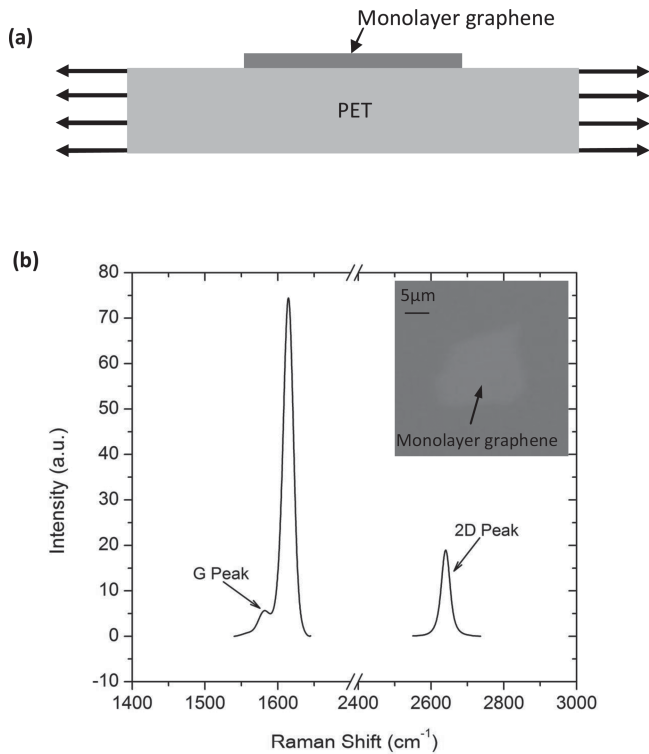
polyethylene terephthalate (PET), using in-situ Raman spectroscopy and atomic force microscopy (AFM). Interfacial sliding under tension and buckling under compression are identified as two limiting mechanisms for stress transfer and coherent integration across the interface. Based on a nonlinear shear-lag model, the interfacial shear strength, the critical strain for onset of interfacial sliding, and stress transfer efficiency are deduced from the measurements.

Raman spectroscopy was used in this study to measure the strain in monolayer graphene on a PET substrate. It has been well established that Raman spectroscopy can be used to measure stress transfer in a variety of composites reinforced with carbon fibers and carbon nanotubes.[12,13] Recent studies have shown that Raman peaks of monolayer graphene shift with deformation, enabling quantitative measurement of strain in graphene.[14,15] Several studies have used graphene on flexible or stretchable substrates, which typically assumed perfect bonding and no sliding at the interface.[16,17] Observation of interfacial sliding was reported for a graphene monolayer sandwiched between PMMA and SU-8 epoxy resin under tension,[18] while indication of graphene buckling on PMMA was reported under compression.[19] In the present work, both interfacial sliding and buckling were observed for the same monolayer graphene on a PET substrate subjected to a uniaxial tensile loading and unloading cycle.

2. Results and Discussion

As illustrated in **Figure 1**a, a PET substrate with graphene flakes on top was mechanically loaded with uniaxil tension by a small-scale mechanical testing stage (Ernest F. Fullam). The Raman spectra of graphene were taken in situ at different levels of applied strain during loading and unloading. Figure 1b shows the Raman spectrum of a monolayer graphene flake on PET before stretching, showing characteristic intensities and waveforms of a monolayer graphene. Since the G peak of graphene partly overlaps with the PET's peak, we rely on the shift of the 2D peak to measure the strain in graphene. **Figure 2**a shows the evolution of the Raman spectra around the 2D peak measured near the center of a graphene flake (Sample #1). The Raman spectra were fitted by Lorentzian functions. Figure 2b

Dr. T. Jiang, Prof. Y. Zhu
Department of Mechanical and Aerospace Engineering
North Carolina State University
Raleigh, NC 27695, USA
E-mail: yong_zhu@ncsu.edu
Prof. R. Huang
Department of Aerospace Engineering
and Engineering Mechanics
University of Texas at Austin
Austin, TX 78712, USA
E-mail: ruihuang@mail.utexas.edu.

Materials Views
www.MaterialsViews.com

ADVANCED
FUNCTIONAL
MATERIALS
www.afm-journal.de

FULL PAPER

Figure 1. (a) Schematic diagram of the experimental setup (cross-sectional view, not to scale). (b) Raman spectrum of a monolayer graphene on a PET substrate. The large peak at 1615 cm^{-1} is from PET background. Inset is an optical image of a monolayer graphene flake.

plots the 2D peak position as a function of the nominal strain applied to the PET substrate. Clearly, the Raman peak started to red shift linearly during loading at a rate of –52.5 cm^{-1}/% until about 2576 cm^{-1}, corresponding to the applied PET strain of ~1.2%. After that, the peak position remained nearly constant. During unloading (e.g., the applied PET strain decreasing), the 2D peak position blue shifted linearly with the PET strain at a rate of –49.4 cm^{-1}/%. Similar Raman peak shift was observed in a PMMA/graphene/SU8 laminate.[17] However, in our experiments, when the PET was stretched up to 7% and then unloaded, the peak shift became nonlinear towards the end of the unloading stage (Sample #2 in Figure 2b). As discussed later, the underlying mechanisms for the observed nonlinear behavior during loading and unloading are attributed to interfacial sliding and buckling.

The measured red/blue shift of the Raman peak can be directly related to the strain (or stress) in the graphene, as a result of stress transfer from PET to graphene across the interface. To understand the interfacial stress transfer, a nonlinear shear-lag analysis was employed (see details in Supporting Information). A conventional shear-lag model assumes a linear elastic response and no interfacial sliding,[18,20] which predicts the strain distribution in the graphene layer, ε_f, as a function of the position, x, along the length direction,

$$\varepsilon_f(x) = \varepsilon_m \left[1 - \frac{\cosh(\beta x)}{\cosh(\beta L/2)} \right] \quad (1)$$
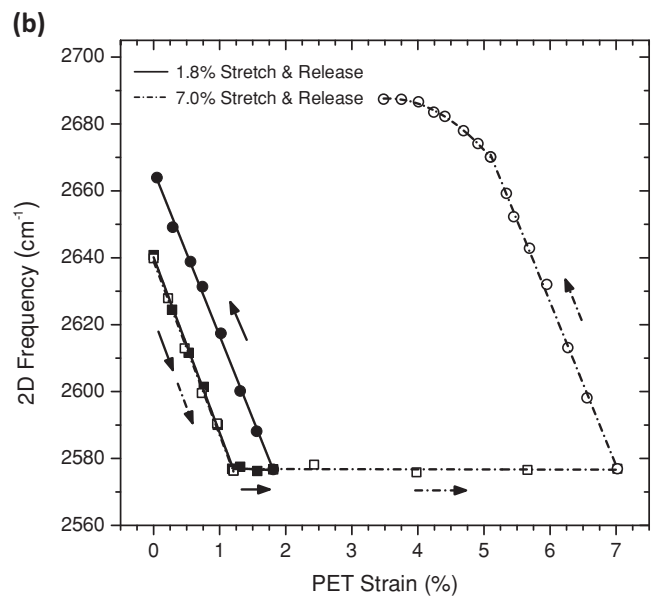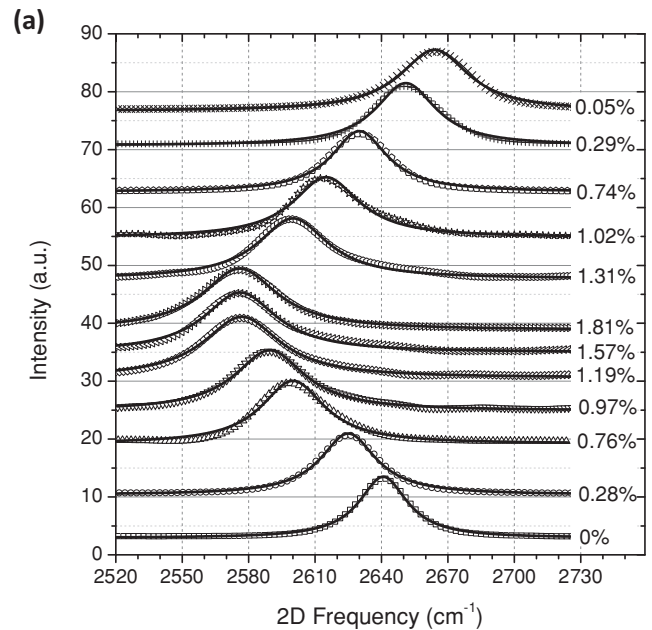
Figure 2. (a) Evolution of the 2D spectrum of a graphene (Sample #1) with the PET strain. The solid lines are Lorentzian fitting of the experimental data (symbols). PET is stretched to 1.81% and then released. (b) 2D peak position versus PET strain for Sample #1 (solid line and symbols) and Sample #2 (dash-dot line and hollow symbols) over a loading/unloading cycle. Symbols ■(□) and ●(○) represent the loading and unloading.

where ε_m is the applied strain to the PET substrate, L is the length of graphene in the x direction with $x = 0$ at the center, and $\beta = \sqrt{\frac{k_m}{E_{2D}}}$ is the shear-lag parameter depending on the effective stiffness of the substrate (k_m) and the in-plane stiffness (or 2D Young's modulus) of monolayer graphene (E_{2D}). The corresponding shear stress, τ, at the graphene-substrate interface is given by

$$\tau(x) = -\beta E_{2D} \varepsilon_m \frac{\sinh(\beta x)}{\cosh(\beta L/2)} \tag{2}$$

By Equations (1) and (2), the maximum strain of graphene occurs at the center ($x = 0$) and the maximum interfacial shear stress occurs at the edges ($x = \pm L/2$). When the interfacial shear stress reaches a critical level (i.e., the interfacial shear strength), interfacial sliding occurs and as a result the strain/stress distributions in the graphene and interface can no longer be predicted by the conventional shear-lag model.[21,22] The onset of interfacial sliding can be predicted by setting the maximum shear stress in Equation (2) equal the interfacial shear strength (τ_c), which corresponds to a critical strain applied to the substrate

$$\varepsilon_c = \frac{\tau_c}{\beta E_{2D}} \coth(\beta L/2) \tag{3}$$

However, this critical strain cannot be directly measured. As shown in Figure S8, the strain at the center of graphene continues increasing almost linearly even after the onset of interfacial sliding ($\varepsilon_m > \varepsilon_c$). As the sliding zones develop from both edges and approach the center (see Figures S4 and S5), the center strain in graphene eventually saturates at a constant level

$$\varepsilon_p = \frac{\tau_c L}{2 E_{2D}} \tag{4}$$

Therefore, the interfacial shear strength can be determined by measuring the plateau strain at the center of the graphene flake. Moreover, it is found that the dimensionless group βL is typically much greater than 1 and as a result the center strain in graphene is approximately equal to the applied strain before it reaches the plateau, e.g., $\varepsilon_f(0) \approx \varepsilon_m$. As shown in Figure 2b, the measured Raman shift reached a plateau when $\varepsilon_m \approx 1.2\%$, which is approximately the plateau strain. By Equation (4) the interfacial shear strength is found to be ~0.7 MPa for Sample #1 ($L = 12.4$ μm) and ~0.5 MPa for Sample #2 ($L = 17.2$ μm), assuming $E_{2D} = 350$ N/m.[23] We note that the obtained interfacial shear strength is comparable to the value reported previouly for a PMMA/graphene/SU8 laminate,[18] while the present work demonstrates a different method for determining the interfacial shear strength. The advantage of the present method is that it requires Raman measurements only at the center of graphene, with no need to map the strain distribution.

To further understand the interfacial stress transfer from PET to graphene, local strains in the graphene along the length direction were measured by Raman at different levels of the applied strain to the PET substrate, as shown in **Figure 3**a. Spatial resolution of 1 μm was obtained for the local strain measurement. To covert the Raman peak shift to strain, the rate of −52.5 cm^{-1}/% was used. It can be seen that the strain builds up in graphene from the edges and approaches a peak at the center where the strain in the graphene approximately equals the applied strain to the PET substrate up to $\varepsilon_m = 1.2\%$. When the applied strain is small (e.g., $\varepsilon_m = 0.2\%$), the strain distribution in graphene is characteristic of the shear-lag effect, as predicted by Equation (1), where the parameter β is commonly treated as an effective measure of the interfacial stress transfer efficiency. By fitting the measured strain distribution at $\varepsilon_m = 0.2\%$ with Equation (1), we obtain $\beta L \approx 10$. As the applied strain increases,
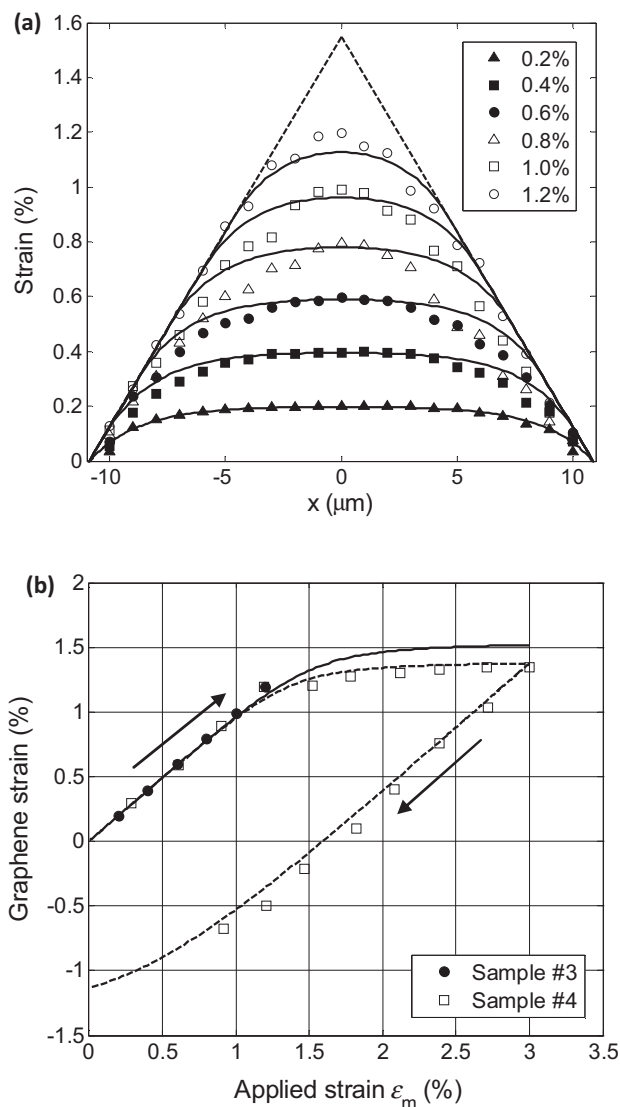
Figure 3. (a) Strain distributions in Sample #3, comparing the Raman measurements (symbols) with the nonlinear shear lag analysis (lines). The dashed lines indicate the limiting case when the center strain reaches the plateau strain as predicted by Equation (4). (b) Center strain in graphene during loading and unloading for Samples #3 and #4, where the plateau strains are slightly different due to different lengths of the graphene flakes in the two samples.

the strain distribution in graphene becomes almost linear near the edges, an evidence of interfacial sliding with a constant shear stress at the interface. By Equation (S1) (i.e., $\frac{d\sigma}{dx} = \tau$), the interfacial shear strength can be determined from the linear slope, which is ~0.5 MPa for this sample (#3). With $L = 21.8$ μm, the critical strain for onset of sliding is $\varepsilon_c \approx 0.3\%$ by Equation (3), while the plateau strain is $\varepsilon_p \approx 1.55\%$ by Equation (4). Using the two parameters ($\beta L = 10$ and $\tau_c = 0.5$ MPa), the strain distributions in graphene are calculated by the nonlinear shear-lag analysis (including interfacial sliding) for $\varepsilon_m = 0.4 - 1.2\%$ and compared with the experimental measurements, as shown in Figure 3a. The overall agreement is excellent despite some local scattering of the experimental data,

www.MaterialsViews.com

ADVANCED
FUNCTIONAL
MATERIALS
www.afm-journal.de

FULL PAPER

Table 1. Summary of the Raman measurements. The interfacial shear strength (τ_c) is calculated by Equation (4) using the measured plateau strain (ε_p) and length (L) along with the 2D Young's modulus of graphene (E_{2D} = 350 N/m). For samples #3 and #4, the shear-lag parameter (βL) is estimated based on the measured strain distributions in graphene, and the critical strain (ε_c) for onset of interfacial sliding is calculated by Equation (3).

Specimen #	Length L [µm]	βL	ε_c	ε_p	τ_c [MPa]
1	12.4	–	–	0.0122	0.689
2	17.2	–	–	0.0122	0.497
3	21.8	10	0.0031	0.0155	0.498
4	16.8	10	0.0028	0.014	0.583
5	19.5	–	–	0.013	0.467
6	13.4	–	–	0.0123	0.643

which strongly supports the hypothesis of interfacial sliding as the underlying mechanism for the observed nonlinear behavior. Moreover, the center strain in graphene is plotted as a function of the applied strain in Figure 3b, showing excellent agreement between the Raman measurements and the nonlinear shear-lag model, including both loading and unloading parts (Samples #3 and #4). Remarkably, while the critical applied strain for onset of sliding is ~0.3% for both samples, the center strain in graphene increases almost linearly with the applied strain up to ~1.2%, far beyond the critical strain. Therefore, the interfacial stress transfer continues after onset of interfacial sliding, but limitted by the plateau strain, which is proportional to the interfacial shear strength and the length of graphene as predicted by Equation (4).

In total, in-situ Raman measurements were performed for six graphene flakes, including the strain distribution measurements for two samples (#3 and #4), while only the center strain was measured for the other samples. The results are summarized in **Table 1**, including the length of the graphene flake (along the loading axis), the plateau strain at the center of the graphene, the interfacial shear strength, and if applicable, the dimensionless group βL and the critial strain for onset of interfacial sliding. Note that the shear-lag parameter β for stress transfer can be determined only for the two samples with strain distribution measurements, while the center strain measurement is sufficient to determine the interfacial shear strength. The interfacial shear strength ranges from 0.46 to 0.69 MPa according to these measurements.

Next we turn attention to the unloading behavior. The interfacial stress transfer leads to tension in the graphene flake as the PET substrate is stretched. Upon unloading, as the PET substrate retracts, the interfacial shear stress is first relaxed and then reversed in opposite directions (see Figure S7). As a result, the graphene flake is increasingly compressed. The nonlinear shear-lag model can be used to predict the unloading behavior including the compressive strain/stress in the graphene flake and reverse sliding along the interface (see Supporting Information). In Figure 2b, it is interesting to note that the linear Raman shift during unloading has a slope nearly identical to that during loading. However, for the sample stretched

to a large strain (e.g., ε_m up to 7%), the Raman shift during unloading became nonlinear beyond a critical point, which corresponds to ~0.7% compressive strain in the graphene. Similar Raman shift was observed in graphene under bending,[19] which was considered as an indication of graphene flake buckling. By the nonlinear shear-lag model, reverse sliding during unloading is predicted, which leads to a nonlinear behavior as shown in Figure 3b. However, other mechanisms may also contribute to the nonlinear behavior observed in experiments. In particular, the compressive strain in the graphene may lead to wrinkling or buckle delamination, which would further relax the compressive strain in the nonlinear regime.

To better understand the unloading behavior, the PET (with graphene on top) was stretched to a series of tensile strains (e.g., 1.9%, 2.0%, 4.0%, and 8.0%), each followed by unloading. AFM images of the graphene flake were taken after each loading-unloading cycle, as shown in **Figure 4**. Notably, while the graphene remained flat after unloading from a small tensile strain (i.e., less than 1.9%), buckling ridges similar to buckle-delamination blisters are observable after the specimen was stretched more than 1.9% and released. The stress-strain curves in Figure S2 show that the tensile strain in PET was fully recovered after unloading to zero stress if the maximum applied tensile strain is lower than ~2%, but not fully recovered for larger tensile strains due to viscoplasticity in PET. Nevertheless, the buckling ridges are observed when the strain recovery exceeds ~1.9% during unloading. Considering that the strain in graphene was tensile during stretching and reached the plateau at ~1.2%, the compressive strain imposed onto the graphene after 1.9% strain recovery in PET would be approximately –0.7%, which is in close agreement with the turning point on the Raman shift (dash–dot curve for Sample 2) as shown in Figure 2b. Therefore, the AFM measurements confirm buckling of the graphene flake under compression and suggest a critical compressive strain of ~–0.7% for buckling of monolayer graphene on PET. Similar critical strain for graphene buckling was inferred previously for graphene on PMMA based on Raman measurements alone.[19] After buckling, the compressive strain in the graphene is released to some extent, which further contributes to the nonlinear behavior during unloading as observed in Figure 2b. The larger the tensile strain applied to the PET, the larger the compressive strain is imposed onto the graphene after unloading, and the more buckling ridges were observed (Figure 4).

Two possible scenarios may lead to buckling of graphene on a substrate, wrinkling or buckle delamination.[24,25] Coincidentally, a critical compressive strain of –0.74% was predicted for strain-induced wrinkling of monolayer graphene on a substrate based on an analytical model of van der Waals interactions.[26] However, no regular wrinkles were observed in the present study. The observed buckling ridges are localized with relatively flat surface between neighboring ridges, characteristic of buckle-delamination blisters,[27,28] although interfacial delamination cannot be confirmed experimentally. The critical strain for buckle delamination in general depends on pre-existing interfacial defects and the substrate stiffness, which can be predicted as

$$\varepsilon_B = \frac{4\pi^2 D}{E_{2D} b_0^2}\zeta \tag{5}$$

FULL PAPER
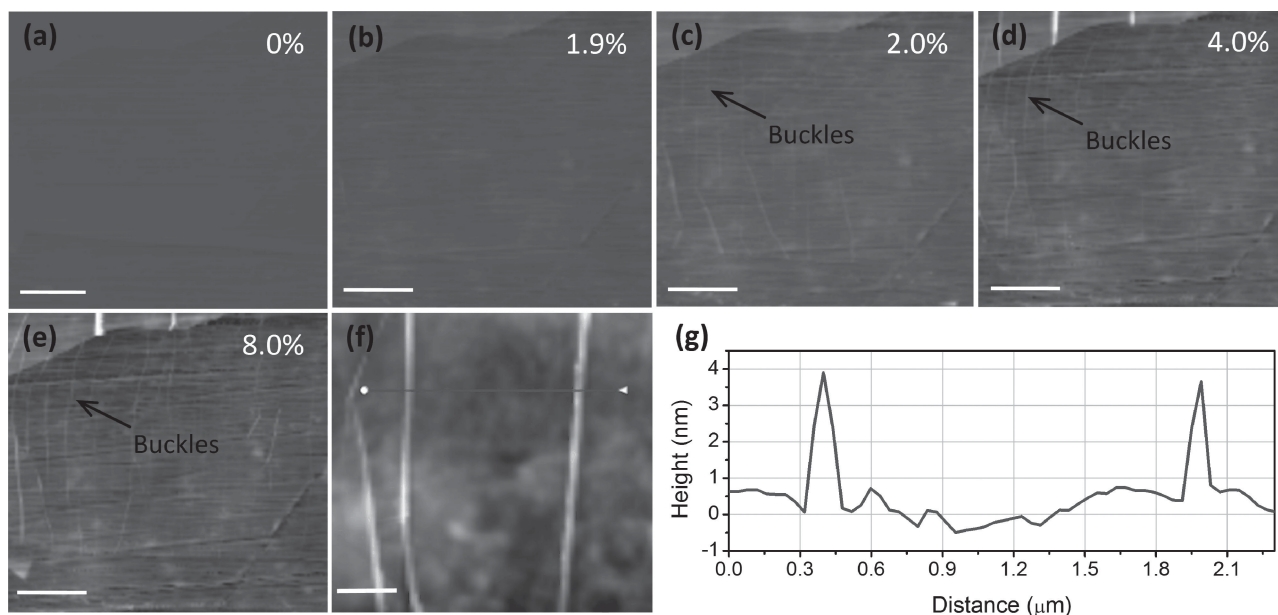
Figure 4. (a–e) AFM images of a graphene flake on PET as the PET underwent four cycles of stretching and releasing. The strain labeled on each image is the maximum tensile strain applied to the PET in each cycle. For stretch below 1.9%, the graphene remained flat (panels a and b), while for stretch larger than 1.9%, buckles were observed (panels c–e). The larger the stretch (from 2% to 8%) of the PET, the larger the compressive strain was imposed on the graphene and the more buckles appeared. Scale bar 10 μm. (f) A high resolution AFM image of the buckles. Scale bar 0.5 μm. (g) Line profile across the buckles on the graphene flake (line in panel f).

where D is the bending modulus of graphene, b_0 is the width of the pre-existing delamination at the interface, and ζ is a dimensionless parameter depending on the relative stiffness of the substrate.[24,29] With E_{2D} = 350 N/m and D = 0.238 nN·nm for monolayer graphene,[23,30] the pre-existing delamination width can be estimated by setting $\varepsilon_B \approx 0.7\%$ and $\zeta \approx 1$, which yields $b_0 \approx 2$ nm. Such interfacial defects could be a result of the graphene placement process and the PET surface roughness. Once buckled, the delamination grows with increasing compressive strain and arrests with the equilibrium size (width and height) depending on the interfacial fracture toughness or adhesion energy. Thus, measurement of the buckle-delamination blisters could offer a potential method for determining the interfacial adhesion energy between graphene and PET.[31,32] From Figure 4g, the width and height of the ridges are estimated to be $b \sim 150$ nm and $h \sim 4$ nm, respectively. Following a fracture mechanics analysis,[31] the interfacial adhesion energy may be determined as

$$\Gamma = \frac{E_{2D}}{2}\left(\frac{\pi}{2}\frac{h}{b}\right)^4 + 8D\left(\frac{\pi}{b}\right)^2\left(\frac{\pi}{2}\frac{h}{b}\right)^2 \qquad (6)$$

which yields an adhesion energy ~0.54 mJ/m². This value is orders of magnitude lower than the adhesion energy reported for graphene on other materials.[33,34] Apparently, the ridge width is likely overestimated from the AFM image. Both the experimental measurement and the theoretical analysis may be improved to determine the adhesion energy more accurately.

It is worthy of noting that the observed buckling ridges in graphene (e.g., Figure 4f) are very similar to the ridge defects commonly formed on epitaxial graphene synthesized by SiC

sublimation method.[35] An AFM image of a graphene with the ridge defects synthesized by the sublimation method is shown in Figure S3 for comparison.[36] Similar ridges (or wrinkles) were found in CVD grown graphene on metal substrates like Ni[37] and Cu.[38] These ridge defects are typically induced by compressive stresses as a result of the difference in thermal expansion coefficients between the graphene and the substrate. The ridge defects on graphene could significantly alter its structural, physical and surface properties.[39–41]

3. Conclusion

Two interfacial failure mechanisms, shear sliding under tension and buckling under compression, were identified experimentally for monolayer graphene on PET using in-situ Raman and AFM measurements. A nonlinear shear-lag model was used to relate the measurements to the interfacial properties including the shear strength and efficiency for stress transfer. The interfacial shear strength was found to range between 0.46 and 0.69 MPa. While the critical strain for onset of interfacial sliding was ~0.3%, the maximum strain that can be transferred to graphene ranged from 1.2% to 1.6% in this work. Upon unloading, the shear-lag model predicts reverse sliding and development of compressive strain/stress in the graphene flake. Beyond a critical compressive strain of around −0.7%, buckling ridges were observed, similar to the ridge defects formed during epitaxial or CVD growth of graphene. The number of buckling ridges increased with increasing compressive strain, which partly relaxed the stress in graphene. The present work on the interfacial mechanics between graphene and PET could provide valuable insight and design guideline for a

broad spectrum of applications of graphene such as flexible and stretchable electronics, strain sensing, and nanocomposites. In addition, for the first time this paper demonstrates a simple experimental method to investigate the graphene/substrate interface under both tension and compression, combining in-situ Raman and AFM measurements. The experimental method can be readily extended to study other two-dimensional nanomaterials (e.g., hexagonal boron nitride, molybdenum disulfide, and silicene) on stretchable substrates.

4. Experimental Section

Sample Preparation: Monolayer graphene flakes were prepared using the mechanical exfoliation method and deposited directly on PET substrates. Prior to depositing graphene flakes, the PET substrates were cleaned with acetone in a supersonic bath, rinsed with isopropanol and deionized water, followed by blown drying with nitrogen gas. Monolayer graphene was determined by its characteristic Raman spectrum and verified by the thickness measurement using an AFM (XE-70, Park Systems).

Raman Characterization: The Raman spectra were measured using a Horiba LabRAM HR system (with a 633 nm laser as the excitation source). The laser power was kept below 0.2 mW to avoid laser-induced local heating of the sample. The incident light was polarized along the strain direction. The objective lens was 100× with a numerical aperture (NA) of 0.9. The focused laser spot was approximately 1 μm in diameter. Figure 1b shows the Raman spectrum and an optical image (inset) of a monolayer graphene flake on PET. For the purpose of comparison, Raman spectrum of a bilayer graphene is shown in Figure S1 (in Supporting Information). In these two figures, the 2D peaks of the Raman spectra exhibit the characteristic intensities and waveforms of a monolayer and bilayer graphene, respectively.

Nonlinear Shear-Lag Analysis with Interfacial Sliding: The critical strain for onset of interfacial sliding is predicted by Equation (3). When $\varepsilon_m > \varepsilon_c$, the interface consists of two sliding zones emerging from the edges and a no-sliding zone in between. Noting the symmetry of the problem, let the sliding zone size to be s at each end. In the sliding zones ($L/2 > |x| > L/2 - s$), the interfacial shear stress and the strain in graphene are

$$\tau = \pm \tau_c \tag{7}$$

$$\varepsilon_f = \frac{\pm \tau_c}{E_{2D}} (x \pm L/2) \tag{8}$$

In the no-sliding zone ($|x| < L/2 - s$), we have

$$\tau = -\frac{\tau_c}{\sinh\left[\beta\left(L/2 - s\right)\right]} \sinh\left(\beta x\right) \tag{9}$$

$$\varepsilon_f = \varepsilon_m - \frac{\tau_c}{\beta E_{2D}} \frac{\cosh\left(\beta x\right)}{\sinh\left[\beta\left(L/2 - s\right)\right]} \tag{10}$$

where the sliding zone size s can be obtained by solving the equation

$$\coth\left[\beta(L/2 - s)\right] + \beta s = \frac{\beta E_{2D}\varepsilon_m}{\tau_c} \tag{11}$$

Details of this analysis are presented in Supporting Information.

Supporting Information

Supporting Information is available from the Wiley Online Library or from the author.

[1] J. S. Bunch, A. M. van der Zande, S. S. Verbridge, I. W. Frank, D. M. Tanenbaum, J. M. Parpia, H. G. Craighead, P. L. McEuen, *Science* **2007**, *315*, 490.

[2] K. Eom, H. S. Park, D. S. Yoon, T. Kwon, *Phys. Rep.* **2011**, *503*, 115.

[3] C. Chen, S. Rosenblatt, K. I. Bolotin, W. Kalb, P. Kim, I. Kymissis, H. L. Stormer, T. F. Heinz, J. Hone, *Nat. Nanotechnol.* **2009**, *4*, 861.

[4] G. Eda, G. Fanchini, M. Chhowalla, *Nat. Nanotechnol.* **2008**, *3*, 270.

[5] K. S. Kim, Y. Zhao, H. Jang, S. Y. Lee, J. M. Kim, K. S. Kim, J.-H. Ahn, P. Kim, J.-Y. Choi, B. H. Hong, *Nature* **2009**, *457*, 706.

[6] T. Ramanathan, A. A. Abdala, S. Stankovich, D. A. Dikin, M. Herrera-Alonso, R. D. Piner, D. H. Adamson, H. C. Schniepp, X. Chen, R. S. Ruoff, S. T. Nguyen, I. A. Aksay, R. K. Prud'Homme, L. C. Brinson, *Nat. Nanotechnol.* **2008**, *3*, 327.

[7] M. A. Rafiee, J. Rafiee, Z. Wang, H. Song, Z.-Z. Yu, N. Koratkar, *ACS Nano* **2009**, *3*, 3884.

[8] S. Stankovich, D. A. Dikin, G. H. B. Dommett, K. M. Kohlhaas, E. J. Zimney, E. A. Stach, R. D. Piner, S. T. Nguyen, R. S. Ruoff, *Nature* **2006**, *442*, 282.

[9] R.-H. Kim, M.-H. Bae, D. G. Kim, H. Cheng, B. H. Kim, D.-H. Kim, M. Li, J. Wu, F. Du, H.-S. Kim, S. Kim, D. Estrada, S. W. Hong, Y. Huang, E. Pop, J. A. Rogers, *Nano Lett.* **2011**, *11*, 3881.

[10] Y. Wang, R. Yang, Z. Shi, L. Zhang, D. Shi, E. Wang, G. Zhang, *ACS Nano* **2011**, *5*, 3645.

[11] X. Huang, Z. Zeng, Z. Fan, J. Liu, H. Zhang, *Adv. Mater.* **2012**, *24*, 5979.

[12] Y. Huang, R. J. Young, *Compos. Sci. Technol.* **1994**, *52*, 505.

[13] S. Cui, I. A. Kinloch, R. J. Young, L. Noé, M. Monthioux, *Adv. Mater.* **2009**, *21*, 3591.

[14] J. Zabel, R. R. Nair, A. Ott, T. Georgiou, A. K. Geim, K. S. Novoselov, C. Casiraghi, *Nano Lett.* **2012**, *12*, 617.

[15] F. Ding, H. Ji, Y. Chen, A. Herklotz, K. Dörr, Y. Mei, A. Rastelli, O. G. Schmidt, *Nano Lett.* **2010**, *10*, 3453.

[16] M. Huang, H. Yan, C. Chen, D. Song, T. F. Heinz, J. Hone, *Proc. Natl. Acad. Sci. USA* **2009**, *106*, 7304.

[17] Z. H. Ni, T. Yu, Y. H. Lu, Y. Y. Wang, Y. P. Feng, Z. X. Shen, *ACS Nano* **2008**, *2*, 2301.

[18] L. Gong, I. A. Kinloch, R. J. Young, I. Riaz, R. Jalil, K. S. Novoselov, *Adv. Mater.* **2010**, *22*, 2694.

[19] G. Tsoukleri, J. Parthenios, K. Papagelis, R. Jalil, A. C. Ferrari, A. K. Geim, K. S. Novoselov, C. Galiotis, *Small* **2009**, *5*, 2397.

[20] Y. Zhu, F. Xu, *Adv. Mater.* **2012**, *24*, 1073.

[21] M. A. Montes-Morán, R. J. Young, *Carbon* **2002**, *40*, 857.

[22] M. Piggott, *Compos. Sci. Technol.* **1991**, *42*, 57.

[23] C. Lee, X. Wei, J. W. Kysar, J. Hone, *Science* **2008**, *321*, 385.

[24] H. Mei, C. M. Landis, R. Huang, *Mech. Mater.* **2011**, *43*, 627.

[25] H. Mei, R. Huang, J. Y. Chung, C. M. Stafford, H.-H. Yu, *Appl. Phys. Lett.* **2007**, *90*, 151902.

[26] Z. H. Aitken, R. Huang, *J. Appl. Phys.* **2010**, *107*, 123531.

[27] D. Vella, J. Bico, A. Boudaoud, B. Roman, P. M. Reis, *Proc. Natl. Acad. Sci. USA* **2009**, *106*, 10901.

[28] G. Parry, J. Colin, C. Coupeau, F. Foucher, A. Cimetière, J. Grilhé, *Acta Mater.* **2005**, *53*, 441.

[29] H.-H. Yu, J. W. Hutchinson, *Int. J. Fract.* **2002**, *113*, 39.

FULL PAPER

[30] K. Kudin, G. Scuseria, B. Yakobson, *Phys. Rev. B* **2001**, *64*, 235406.

[31] S. Faulhaber, C. Mercer, M. Moon, J. W. Hutchinson, A. G. Evans, *J. Mech. Phys. Solids* **2006**, *54*, 1004.

[32] Y. Aoyanagi, J. Hure, J. Bico, B. Roman, *Soft Matter* **2010**, *6*, 5720.

[33] S. P. Koenig, N. G. Boddeti, M. L. Dunn, J. S. Bunch, *Nat. Nanotechnol.* **2011**, *6*, 543.

[34] T. Yoon, W. C. Shin, T. Y. Kim, J. H. Mun, T.-S. Kim, B. J. Cho, *Nano Lett.* **2012**, *12*, 1448.

[35] N. Srivastava, G. He, R. M. Feenstra, P. J. Fisher, *Phys. Rev. B* **2010**, *82*, 235406.

[36] G. Prakash, M. Capano, M. Bolen, D. Zemlyanou, R. Reifenberger, *Carbon* **2010**, *48*, 2383.

[37] A. N. Obraztsov, E. A. Obraztsova, A. V. Tyurnina, A. A. Zolotukhin, *Carbon* **2007**, *45*, 2017.

[38] X. Li, W. Cai, J. An, S. Kim, J. Nah, D. Yang, R. Piner, A. Velamakanni, I. Jung, E. Tutuc, S. K. Banerjee, L. Colombo, R. S. Ruoff, *Science* **2009**, *324*, 1312.

[39] K. Xu, P. Cao, J. R. Heath, *Nano Lett.* **2009**, *9*, 4446.

[40] W. Zhu, T. Low, V. Perebeinos, A. A. Bol, Y. Zhu, H. Yan, J. Tersoff, P. Avouris, *Nano Lett.* **2012**, *12*, 3431.

[41] J. Zang, S. Ryu, N. Pugno, Q. Wang, Q. Tu, M. J. Buehler, X. Zhao, *Nat. Mater.* **2013**, *12*, 321.